

west Ophthalmol Vis Sci. Author manuscript; available in PMC 2009 September 14.

Published in final edited form as:

Invest Ophthalmol Vis Sci. 2008 November; 49(11): 5103-5110. doi:10.1167/iovs.08-2127.

Ultrahigh-Speed Optical Coherence Tomography for Three-Dimensional and En Face Imaging of the Retina and Optic Nerve Head

Vivek J. Srinivasan 1 , Desmond C. Adler 1 , Yueli Chen 1,2 , Iwona Gorczynska 1,2 , Robert Huber 1,3 , Jay S. Duker 2 , Joel S. Schuman 4 , and James G. Fujimoto 1

¹Department of Electrical Engineering and Computer Science and Research Laboratory of Electronics, Massachusetts Institute of Technology, Cambridge, Massachusetts

²New England Eye Center, Tufts Medical Center, Tufts University, Boston, Massachusetts

³Lehrstuhl für BioMolekulare Optik, Ludwig-Maximilians-Universität München, Fakultät für Physik, Munich, Germany

⁴UPMC Eye Center, Department of Ophthalmology, University of Pittsburgh, School of Medicine, Pittsburgh, Pennsylvania

Abstract

Purpose—To demonstrate ultrahigh-speed optical coherence tomography (OCT) imaging of the retina and optic nerve head at 249,000 axial scans per second and a wavelength of 1060 nm. To investigate methods for visualization of the retina, choroid, and optic nerve using high-density sampling enabled by improved imaging speed.

Methods—A swept-source OCT retinal imaging system operating at a speed of 249,000 axial scans per second was developed. Imaging of the retina, choroid, and optic nerve were performed. Display methods such as speckle reduction, slicing along arbitrary planes, en face visualization of reflectance from specific retinal layers, and image compounding were investigated.

Results—High-definition and three-dimensional (3D) imaging of the normal retina and optic nerve head were performed. Increased light penetration at 1060 nm enabled improved visualization of the choroid, lamina cribrosa, and sclera. OCT fundus images and 3D visualizations were generated with higher pixel density and less motion artifacts than standard spectral/Fourier domain OCT. En face images enabled visualization of the porous structure of the lamina cribrosa, nerve fiber layer, choroid, photoreceptors, RPE, and capillaries of the inner retina.

Conclusions—Ultrahigh-speed OCT imaging of the retina and optic nerve head at 249,000 axial scans per second is possible. The improvement of \sim 5 to $10\times$ in imaging speed over commercial spectral/Fourier domain OCT technology enables higher density raster scan protocols and improved performance of en face visualization methods. The combination of the longer wavelength and ultrahigh imaging speed enables excellent visualization of the choroid, sclera, and lamina cribrosa.

Corresponding author: James G. Fujimoto, Department of Electrical Engineering and Computer Science and Research Laboratory of Electronics, Massachusetts Institute of Technology 77 Massachusetts Avenue, Cambridge, MA 02139; jgfuji@mit.edu.

Presented at the annual meeting of the Association for Research in Vision and Ophthalmology, Fort Lauderdale, Florida, May 2007.

Disclosure: V.J. Srinivasan, None; D.C. Adler, None; Y. Chen, None; I. Gorczynska, None; R. Huber, LightLab Imaging (P); J.S. Duker, None; J.S. Schuman, Carl Zeiss Meditec (P), LightLab Imaging (P); J.G. Fujimoto, Carl Zeiss Meditec (P), LightLab Imaging (P), Optovue (C, I)

Optical coherence tomography (OCT) is an emerging optical imaging modality for biomedical research and clinical medicine. In the eye, OCT can provide detailed images of retinal diseases including diabetic retinopathy, age-related macular degeneration, and glaucoma. The commercial StratusOCT instrument (Carl Zeiss Meditec, Inc., Dublin, CA), with 8- to 10- μ m axial image resolution, has become a standard in the diagnosis and monitoring of diseases such as wet age-related macular degeneration, diabetic macular edema, and glaucoma.

Recent work in the field of ophthalmic OCT has demonstrated that spectral/Fourier domain detection methods^{4–7} enable OCT imaging with dramatically improved speed and sensitivity over conventional time domain methods.^{8–10} Spectral/Fourier domain OCT uses a broadband light source and a spectrometer to measure the interference spectrum. Light backscattered or backreflected from different positions in the sample is measured simultaneously, rather than sequentially, improving the imaging speed. The improved speed enables three-dimensional (3D) and high-definition imaging of the retina and enhanced visualization of retinal diseases. ^{11–14} Several companies have developed clinical spectral/Fourier domain OCT instruments for retinal imaging. These instruments operate at speeds of 20,000 to 40,000 axial scans per second, 50 to 100 times faster than previous OCT instruments.

Despite the dramatically improved performance of spectral/Fourier domain OCT, there are several important limitations. First, spectral/Fourier domain detection utilizes a high-speed camera and spectrometer for detection, which increases system size and complexity. Second, because of spectrometer and camera resolution limits, detection sensitivity and axial resolution change as a function of axial position or imaging depth. ^{7,8,15} This sensitivity decrease may adversely affect the reproducibility of quantitative measurements. Finally, spectrometer losses and camera read out rates limit the maximum imaging speed.

Therefore, although 3D imaging with spectral/Fourier domain OCT is possible, motion artifacts prevent reliable acquisition of 3D data sets when high sampling density is desired. For example, at an acquisition speed of 25,000 axial scans per second, a raster scan of the macula consisting of 512 × 512 axial scans would require >10 seconds. Current ophthalmic systems solve this problem by sacrificing sampling density along one axis of the raster scan or individually acquiring densely sampled data sets from different portions of the retina. The first approach does not adequately sample the retina, and the second approach requires the precise acquisition and registration of multiple data sets, which may be time-consuming and cumbersome in subjects with poor fixation. Some commercially available, high-end OCT instruments provide active eye motion tracking that enables long acquisition times and high-density data sets. However, eye tracking requires an additional optical system to determine eye motion and actuators to correct for eye motion, both of which increase system complexity and cost.

Swept-source OCT^{10,16–19} is another approach for high-speed OCT imaging which possesses speed and sensitivity advantages similar to those of spectral/Fourier domain OCT. Both methods measure interference as a function of optical frequency or wavelength. However, swept-source OCT uses a frequency swept laser that enables measurement of interference at different optical frequencies or wavelengths sequentially over time. Swept-source OCT imaging of the retina was first demonstrated in 2006 at 18,800 axial scans per second and 14- μ m axial resolution in air, using a 1050-nm frequency swept laser.²⁰ Swept-source OCT imaging of the human retina was also demonstrated at 43,200 axial scans per second and 13 μ m axial resolution in air, using an 850-nm frequency swept laser.²¹ and 16,000 axial scans per second and 9.5- μ m axial resolution in air using an 850-nm frequency swept laser.²² Recently, swept-source OCT imaging of the human retina was demonstrated at 28,000 axial scans per second and 14.4- μ m axial resolution in air with a 1050-nm frequency swept laser.²³ Our group previously demonstrated swept-source OCT imaging at 236,000 axial scans per second and 19- μ m axial resolution in air with a 1060-nm Fourier domain mode locked (FDML)

frequency swept laser. ²⁴ In this article, OCT imaging of the retina and optic nerve head at 249,000 axial scans per second and 11- μ m axial resolution in air (8 μ m in the retina) are demonstrated.

Methods

Figure 1A illustrates the concept of swept-source OCT. An optical frequency sweep is incident on the Michelson interferometer and split between the sample and reference arms. In this example, the optical frequency varies linearly over time. Because of the path length difference $2\Delta L$ between the two arms of the interferometer, the frequency sweep reflected from the sample arm (Fig. 1, dotted line) is delayed relative to the frequency sweep reflected from the reference arm (Fig. 1, dashed line). The two frequency sweeps interfere on the detector, which detects the average intensity as a function of time. Because the two frequency sweeps are delayed with respect to each other, there is a frequency difference between light from the sample arm and light from the reference arm, which results in a beat frequency in the intensity. For a linear frequency sweep, the beat frequency is proportional to the path length delay; therefore, the echo time delay can be measured by Fourier transforming this beat frequency signal.

All frequency swept lasers consist of a gain element, a tunable filter, and a feedback mechanism. For conventional swept laser designs, the sweep speed is limited because when the laser is tuned to a new frequency, it is necessary to build up lasing from amplified spontaneous emission at the new frequency and attenuate light at the old frequency. ²⁵ To overcome these limitations, a new approach called Fourier domain mode locking (FDML) has been developed that enables a dramatic increase in OCT imaging speeds. ²⁶ FDML lasers achieve improved performance compared with conventional swept lasers by using an optical fiber delay line in the laser cavity and synchronizing the sweep speed of the tunable filter in the laser to the roundtrip time of the light inside the laser cavity.

Figure 1B shows a schematic of the FDML laser. A fiberoptic Fabry-Perot tunable filter (FFP-TF; Micron Optics, Inc. Atlanta, GA) with a line width of 0.08 nm is used to filter the light propagating in the cavity. A semiconductor optical amplifier (InPhenix, Livermore, CA) is used as the gain element; 825 m of optical fiber is used as the cavity. The fiber is on a spool, and the entire laser can be made compact. The filter is tuned at the round-trip frequency of ~124.5 kHz. As described previously, the semiconductor optical amplifier (SOA) is turned off during the forward (short- to long-wavelength) sweep, and an extra-cavity unbalanced Mach-Zehnder is used to double the repetition rate. ²⁴ The new features of the laser reported herein include the sigma ring cavity with a Faraday mirror (FM) and circulator (CIRC), and the intracavity unbalanced Mach-Zehnder. This new design enables improved noise performance, stability, and image quality, as well as improved imaging speed and resolution.

The OCT system schematic is shown in Figure 1C. The frequency sweep is split between the OCT interferometer, a reference Mach-Zehnder interferometer (MZI) used to recalibrate the acquired fringes in software, and an optical spectrum analyzer (OSA), used to monitor the time-averaged spectrum. The OCT interferometer consists of a slit lamp platform for imaging the retina and a reference path. Dual-balanced detection was used to cancel excess intensity noise. To enable continuous data acquisition, the 14-bit, 200-MHz acquisition card (GaGe CompuScope 14,200) was triggered only once at the beginning of data acquisition to eliminate the downtime required for trigger rearming. The long record was divided into individual sweeps by postprocessing software. The axial resolution was 11 μ m in air (8 μ m in tissue), and the sensitivity was 91 dB for an incident power of 1.2 mW. The incident exposure levels were consistent with the safe exposure determined by ANSI standards.

For this study, two normal subjects (one 27-year-old man and one 35-year-old man) were imaged at the Massachusetts Institute of Technology (MIT). The study was approved by the MIT Institutional Review Board. Written informed consent was obtained from all subjects before OCT imaging was performed. The research adhered to the tenets of the Declaration of Helsinki.

Several scan protocols were used. The first generated single high-definition cross-sectional images with 16,000 axial scans. Each image could be acquired in approximately 0.064 seconds. The second was a 3D raster pattern with 512 images \times 425 axial scans per frame and required 1 second. The third was a 3D raster pattern with 512 images \times 850 axial scans per image and required 2 seconds. For raster scans, the fast scan axis was the horizontal (temporal-nasal) one, and the slow axis was the vertical (inferior-superior) one. In addition, imaging was performed with two different transverse resolutions, by using two different ocular lenses with focal lengths of 25 and 50 mm, resulting in beam diameters of 1.4 and 2.9 mm on the cornea, respectively. For the 1.4-mm beam diameter, the transverse resolution for retinal imaging was approximately 21 μ m, whereas for the 2.9-mm beam diameter, the transverse resolution was approximately 10 to 15 μ m, depending on the ocular aberrations. The captions for Figures 2–7 indicate the beam diameter and scan protocol used.

Various visualization and image processing methods were investigated for viewing retinal anatomy. Three-dimensional rendering, image slicing at arbitrary planes, filtering to reduce speckle, and en face visualization of selected retinal layers were investigated. Three-dimensional rendering and image slicing were performed (Amira 3.1; Mercury Computer Systems, Inc., Chelmsford, MA) rendering software. For raster scans of the macula and optic nerve head, 3D OCT data sets were corrected for axial motion by cross-correlation of consecutive images from the raster scan. Axial motion during acquisition of a single cross-sectional image was assumed to be negligible.

For en face visualization, the inner segment/outer segment junction (IS/OS) and vitreoretinal interface were first detected by software. The nerve fiber layer (NFL) around the fovea was visualized by computing the median reflectance from the vitreoretinal interface to the region 30-µm posterior to the vitreoretinal interface. The retinal vessels in the ganglion cell layer (GCL) were visualized by using a surface to approximate the contour of the ganglion cell layer. To compute the retinal vessel image, each axial scan was multiplied by a Gaussian window $(\sigma = 25 \,\mu\text{m})$ centered on this layer, and a maximum projection filter was applied along the axial direction. The capillaries of the inner nuclear layer were visualized by using a surface to approximate the contour of the inner nuclear layer. To compute the capillary image, each axial scan was multiplied by a Gaussian window ($\sigma = 25 \mu m$) centered on this layer, and a maximum projection filter was applied along the axial direction. The foveal avascular zone was detected based on the foveal contour and excluded from the image. The photoreceptors, RPE, and choroid were also visualized by axial integration over the corresponding regions.²⁰ Speckle reduction was accomplished by up-sampling the complex images from a 3D OCT data set in the axial direction by a factor of 4, computing the absolute value, correlating consecutive frames to remove relative displacements, and forming a filtered image consisting of the median of the absolute values of the individual images.

Results

Figure 2 shows high definition images of the retina consisting of 16,000 axial scans per image. The foveal image (Fig. 2A) shows all major retinal layers. The image of the optic nerve head (Fig. 2B) shows light penetration to the deeper structures of the optic nerve head. Both images show excellent visualization of the choroid. Figure 3 shows 3D OCT fundus imaging, ^{28–30} and image slicing along arbitrary planes, with and without motion correction. Figure 3A shows

an OCT fundus image of the macular region, exhibiting no apparent transverse motion artifacts. Figure 3B shows a nasal–temporal image, parallel to the fast axis of the raster scan, which takes approximately 0.0034 seconds to acquire. Because of the rapid acquisition, no axial motion artifacts are visible. Figure 3C shows an orthogonal slice through the 3D OCT data along the inferior–superior direction, parallel to the slow axis of the raster scan. Axial motion artifacts are evident. Figure 3D shows the same image after high-frequency motion correction. Although this image is interpolated from the 3D OCT data set, the high sampling density yields an image comparable to the fast axis image (Fig. 3B). Figure 3E shows an OCT fundus image of the optic nerve head, without motion correction, again exhibiting no apparent transverse motion artifacts. Figure 3F shows an oblique slice through the 3D OCT data set, after correcting for axial motion.

Figure 4 shows en face visualization of the inner retina. A foveal image (Fig. 4A) and parafoveal image (Fig. 4B) are shown with the boundaries delineated. By using the boundaries to process the 3D OCT data set, as described in the Methods section, the NFL (Fig. 4C, 4F), GCL vessels (Fig. 4D, 4G), and inner nuclear layer capillaries (Fig. 4E, 4H) are visualized. Figure 5 shows en face visualization of the outer retina and choroid. An OCT cross-sectional image is shown with a white line outlining the contour of Bruch's membrane (Fig. 5A). Different layers are visualized by axial integration of the signal amplitude over different ranges relative to this contour (Figs. 5B–D). Figure 6 shows the effects of image compounding by median filtering. While intraretinal layers are visible in a single cross-sectional image (Fig. 6A), they are not clearly delineated due to speckle. The results of compounding of 2 (Fig. 6B), 6 (Fig. 6C), and 12 (Fig. 6D) images are shown. Although a significant improvement is seen between compounding one image (Fig. 6A) and compounding two images (Fig. 6B), after compounding six images (Fig. 6C) a point of diminishing returns is reached. Little difference is seen between 6 (Fig. 6C) and 12 (Fig. 6D) images.

Figures 7A–B show visualization of the lamina cribrosa by interpolating 3D OCT data onto en face planes. Figure 7B shows a trend of decreasing pore size with increasing depth relative to the RPE, larger pore size in the superior and inferior portions of the lamina relative to the other portions, and increasing pore size with increasing distance from the center of the optic disc. All trends are consistent with known anatomy. ^{31,32} Figure 7C shows a single image from the median filtering six consecutive images along the slow axis. The lamina cribrosa (LC) is clearly visible in this cross-sectional image.

Discussion

Although spectral/Fourier domain OCT technology operates at speeds of 20,000 to 40,000 axial scans per second, imaging performance is limited in practice by the relatively long times needed to acquire dense 3D OCT data sets. In this study, OCT imaging speeds of 249,000 axial scans per second were demonstrated, which is almost an order of magnitude faster than commercial spectral/Fourier domain OCT systems.

Several papers have demonstrated applications of high-speed imaging including 3D imaging, high-definition imaging, and quantitative mapping. ^{11–14},³³ The advances in imaging speed reported herein have the potential to improve the performance of these scan protocols in the ophthalmology clinic. The demonstrated improvements in imaging speed will reduce motion artifacts significantly in patients with tear film dysfunction, short attention, excessive blinking, or gross tremor. The 1060-nm center wavelength should improve imaging through dense or opaque media, and enhance visualization of the choroid, an effect first demonstrated with time-domain OCT³⁴,³⁵ and later with spectral/Fourier domain OCT. ³⁶ An added benefit of the longer wavelength is that the beam scanning on the retina is virtually invisible to the subject and therefore does not pose a distraction. Although water absorption in the ocular media has the

potential to reduce sensitivity for retinal imaging, permissible exposure levels are higher at 1060 nm compared with 800 nm and help to offset water absorption.

In addition to improving performance of existing scan patterns, the advances in imaging speed presented herein enable very dense raster scanning protocols. The OCT fundus image generated from these dense raster scanning protocol has excellent quality due to the high transverse pixel density, as shown in Figures 3A and 3E. The results illustrate that axial motion is present in 3D OCT data sets (Fig. 3C). However, with axial motion correction it is possible to achieve high quality cross-sections at any orientation (Figs. 3D, 3F).

3D OCT data sets in Figure 3 were corrected for axial motion by cross-correlation of consecutive images from the raster scan. This approach is similar to the approach of the StratusOCT instrument, which cross-correlates consecutive axial scans. Cross-correlation of consecutive images improves motion correction compared with correlation of consecutive axial scans. In an ultrahigh-speed, densely sampled 3D OCT data set, consecutive images are acquired in a short period and are highly correlated due to their close transverse spacing. Cross-correlation corrects local motion artifacts well, effectively removing undulations in the vitreoretinal interface and RPE caused by eye motion, as shown in Figures 3D and 3F. However, cross-correlation may not recover the larger scale retinal contour in the vertical direction. Retinal contour is preserved in the horizontal direction, because the imaging speed is so rapid that negligible eye motion occurs during acquisition of a single cross-sectional image. Alternative approaches to motion correction are possible, such as the use of vertical registration scans perpendicular to the fast horizontal axis of the raster scan. In the future, the performance of different eye motion correction algorithms must be clinically validated in eyes with retinal diseases.

Image compounding by median filtering can be used to reduce speckle and improve visualization of the outer retina as shown in Figure 6. In addition, it can be used to improve visualization of deeper structures in the optic nerve head, such as the lamina cribrosa (Fig. 7C). Although previous studies have demonstrated the use of retinal tracking and image averaging to reduce speckle,³⁷ they depend on small eye movements to decorrelate speckle in multiple images. In this study, due to the ultrahigh imaging speed, multiple images can be rapidly acquired at different transverse positions before the eye has moved significantly, which should enable more controlled and repeatable speckle reduction.

The 3D data can also be processed in various ways to generate en face images. High-quality en face visualizations require very high-density 3D OCT data sets since each pixel in the en face image requires one axial scan. The advantage of en face images is that they condense information from the 3D OCT data set, and enable assessment of microstructure which would not otherwise be visible. En face visualization of the NFL bundles (Figs. 4C, F), GCL vessels (Figs. 4D, G), INL capillary network (Figs. 4E, 4H), photoreceptors and RPE (Fig. 5B), choroid (Figs. 5C, 5D) and the lamina cribrosa (Fig. 7B) was demonstrated. In addition to this study, previous spectral/Fourier domain OCT studies have demonstrated similar methods of en face visualization of individual retinal layers ^{12,20,30,38} (Ishikawa H, et al. *IOVS* 2008;49:ARVO E-Abstract 1886). These methods differ from traditional en face OCT, which is a time-domain method providing en face images of the retina. ^{39–43} En face OCT typically acquires individual transverse priority images at one axial depth, which may intersect multiple layers of the retina depending on how the retina is tilted. Swept source/Fourier domain OCT imaging speed enables acquisition of a densely sampled volumetric data set that can be processed to create en face images by using flexible image-processing methods to increase the contrast of or selectively display the layers of interest.

One hypothesis for the pathogenesis of glaucoma is that intraocular pressure causes stress and strain resulting in mechanical failure of the connective tissues of the lamina cribrosa, scleral canal wall, and peripapillary sclera. ⁴⁴ Therefore, in vivo measurements of the lamina cribrosa and connective tissues may aid in the understanding of glaucoma pathogenesis. Our results show that the longer wavelength and capability for image compounding enabled by ultrahigh imaging speeds may improve visualization of these structures.

Typically, the lamina cribrosa is not visible in normal eyes in standard fundus photographs. In glaucoma, neural damage exposes more of the lamina cribrosa surface, which makes the lamina funduscopically visible. This enables quantification of parameters such as pore size and shape in standard clinical photographs. A recent longitudinal study showed that individual pore size (mean pore-to-disc area ratio) decreased between baseline and follow-up $(3.9 \pm 0.7 \text{ years})$ measurements of glaucomatous eyes. ⁴⁵ Although it is possible to evaluate the inner surface of the lamina cribrosa funduscopically, the outer layers of this structure may have different morphology. Therefore, a method of 3D imaging is required. In addition, it is desirable to visualize structures such as the scleral canal and flange tissue, the sclera, and pial sheath. ⁴⁶ This requires an imaging method with high sensitivity and capability to image the deeper portions of the sclera and lamina cribrosa.

Scanning laser ophthalmoscopes (SLO) have been used to perform morphometric measurements on the lamina cribrosa in normal and glaucomatous eyes. ^{47–49} The SLO uses confocal detection to suppress light backscattered from axial positions outside of the focal plane. With standard implementations of this technology, confocality is limited by ocular aberrations. The adaptive optics SLO has therefore been used to achieve improved axial (longitudinal) resolution and image contrast in the presence of ocular aberrations. ⁵⁰ OCT, by comparison, achieves axial resolution by using low coherence interferometry, and typically achieves larger penetration depths than confocal detection alone. The lamina cribrosa has been visualized using en face OCT with dynamic focusing. ⁵¹ Although this method achieves high speed and transverse resolution, consecutive en face images may not be precisely registered due to axial eye motion, and therefore 3D morphology is difficult to assess. The 3D imaging capability demonstrated herein enables visualization of the laminar morphology at depths precisely registered to the RPE (Fig. 7B), which may eventually facilitate quantitative volumetric measurements.

Although motion artifacts are reduced at imaging speeds of 249,000 axial scans per second, the data sets are still not free from eye motion. Eye motion can result from tremor, drifts, and microsaccades. Tremor and drifts have small amplitudes of $<50 \,\mu\text{m}$, whereas microsaccades can cause rapid displacements of several hundred micrometers in 25 ms. Microsaccades generally occur at <5-Hz frequency, but are dependant on conditions. Axial motion is also clearly present in the 3D OCT data sets, as shown in Figure 3C. Therefore, further improvements in imaging speed are desirable to reduce motion artifacts. By increasing interferometer detection efficiency and increasing the average power incident on the cornea to approximately 3.3 mW³⁵ swept-source OCT technology will scale to 500,000 to 1,000,000 axial scans per second with comparable sensitivity. Presently, higher speed line scan CCD cameras are becoming available with speeds of 300 kHz, and therefore spectral/Fourier domain OCT may be an alternative method of achieving ultrahigh imaging speeds. However, swept-source OCT has the potential to achieve more efficient detection and better sensitivity, which may ultimately make it the preferred technology for imaging at very high speeds.

In conclusion, OCT imaging of the retina was demonstrated at 249,000 axial scans per second, a factor of \sim 5 to 10 times higher speed than commercial spectral/Fourier domain OCT technology. The results presented herein demonstrate that high-quality imaging of the retina is possible even at ultrahigh imaging speeds. The ultrahigh imaging speeds enable high-density

sampling for improved en face visualization of the architectural morphology of the retina and optic nerve head such as the nerve fiber layer bundles, intraretinal layer blood vessels and capillary network, photoreceptors, RPE, and the lamina cribrosa. The combination of the longer wavelength and ultrahigh imaging speed enables excellent visualization of the choroid, sclera, and lamina cribrosa.

Acknowledgments

Supported by National Eye Institute Grants R01-EY11289-21, R01-EY13178-07, and P30-EY008098; National Science Foundation Grant BES-0522845; Air Force Office of Scientific Research, Medical Free Electron Laser Program Contract FA9550-07-1-0101; Massachusetts Lions Eye Research Fund; The Eye and Ear Foundation of Pittsburgh; and a Research to Prevent Blindness unrestricted grant. VS was supported by a National Science Foundation Graduate Research Fellowship. DCA received support from the Natural Sciences and Engineering Research Council of Canada. RH was supported by the Emmy Noether program of the German Foundation (DFG) HU 1006/2-1.

References

- 1. Huang D, Swanson EA, Lin CP, et al. Optical coherence tomography. Science 1991;254(5035):1178–1181. [PubMed: 1957169]
- 2. Puliafito CA, Hee MR, Lin CP, et al. Imaging of macular diseases with optical coherence tomography. Ophthalmology 1995;102(2):217–229. [PubMed: 7862410]
- Schuman, JS.; Puliafito, CA.; Fujimoto, JG. Optical Coherence Tomography of Ocular Diseases. Vol. 2nd. Thorofare, NJ: Slack Inc.; 2004.
- 4. Fercher AF, Hitzenberger CK, Kamp G, Elzaiat SY. Measurement of intraocular distances by backscattering spectral interferometry. Opt Commun 1995;117(1–2):43–48.
- 5. Häusler G, Lindner MW. "Coherence radar" and "spectral radar": new tools for dermatological diagnosis. J Biomed Opt 1998;3(1):21–31.
- 6. Wojtkowski M, Bajraszewski T, Targowski P, Kowalczyk A. Real-time in vivo imaging by high-speed spectral optical coherence tomography. Opt Lett 2003;28(19):1745–1747. [PubMed: 14514087]
- 7. Nassif NA, Cense B, Park BH, et al. In vivo high-resolution video-rate spectral-domain optical coherence tomography of the human retina and optic nerve. Opt Express 2004;12(3):367–376. [PubMed: 19474832]
- 8. Leitgeb R, Hitzenberger CK, Fercher AF. Performance of Fourier domain vs. time domain optical coherence tomography. Opt Express 2003;11(8):889–894. [PubMed: 19461802]
- 9. de Boer JF, Cense B, Park BH, et al. Improved signal-to-noise ratio in spectral-domain compared with time-domain optical coherence tomography. Opt Lett 2003;28(21):2067–2069. [PubMed: 14587817]
- Choma MA, Sarunic MV, Yang C, Izatt J. Sensitivity advantage of swept source and Fourier domain optical coherence tomography. Opt Express 2003;11(18):2183–2189. [PubMed: 19466106]
- 11. Schmidt-Erfurth U, Leitgeb RA, Michels S, et al. Three-dimensional ultrahigh-resolution optical coherence tomography of macular diseases. Invest Ophthalmol Vis Sci 2005;46(9):3393–3402. [PubMed: 16123444]
- 12. Wojtkowski M, Srinivasan V, Fujimoto JG, et al. Three-dimensional retinal imaging with high-speed ultrahigh-resolution optical coherence tomography. Ophthalmology 2005;112(10):1734–1746. [PubMed: 16140383]
- 13. Chen TC, Cense B, Pierce MC, et al. Spectral domain optical coherence tomography: ultra-high speed, ultra-high resolution ophthalmic imaging. Arch Ophthalmol 2005;123(12):1715–1720. [PubMed: 16344444]
- 14. Srinivasan VJ, Wojtkowski M, Witkin AJ, et al. High-definition and 3-dimensional imaging of macular pathologies with high-speed ultrahigh-resolution optical coherence tomography. Ophthalmology 2006;113(11):2054, e1–e14. [PubMed: 17074565]
- 15. Wojtkowski M, Srinivasan VJ, Ko TH, et al. Ultrahigh-resolution, high-speed, Fourier domain optical coherence tomography and methods for dispersion compensation. Opt Express 2004;12(11):2404–2422. [PubMed: 19475077]

16. Golubovic B, Bouma BE, Tearney GJ, Fujimoto JG. Optical frequency-domain reflectometry using rapid wavelength tuning of a Cr4+: forsterite laser. Opt Lett 1997;22(22):1704–1706. [PubMed: 18188341]

- 17. Chinn SR, Swanson EA, Fujimoto JG. Optical coherence tomography using a frequency-tunable optical source. Opt Lett 1997;22(5):340–342. [PubMed: 18183195]
- 18. Yun SH, Tearney GJ, de Boer JF, Iftimia N, Bouma BE. High-speed optical frequency-domain imaging. Opt Express 2003;11(22):2953–2963. [PubMed: 19471415]
- 19. Yun SH, Boudoux C, Pierce MC, et al. Extended-cavity semiconductor wavelength-swept laser for biomedical imaging. IEEE Photon Technol Lett 2004;16(1):293–295.
- 20. Lee ECW, de Boer JF, Mujat M, Lim H, Yun SH. In vivo optical frequency domain imaging of human retina and choroid. Opt Express 2006;14(10):4403–4411. [PubMed: 19516592]
- 21. Lim H, Mujat M, Kerbage C, et al. High-speed imaging of human retina in vivo with swept-source optical coherence tomography. Opt Express 2006;14(26):12902–12908. [PubMed: 19532183]
- Srinivasan VJ, Huber R, Gorczynska I, et al. High-speed, high-resolution optical coherence tomography retinal imaging with a frequency swept laser at 850 nm. Opt Lett 2007;32(4):361–363.
 [PubMed: 17356653]
- 23. Yasuno Y, Hong YJ, Makita S, et al. In vivo high-contrast imaging of deep posterior eye by 1-mu m swept source optical coherence tomography and scattering optical coherence angiography. Opt Express 2007;15(10):6121–6139. [PubMed: 19546917]
- 24. Huber R, Adler DC, Srinivasan VJ, Fujimoto JG. Fourier domain mode locking at 1050 nm for ultrahigh-speed optical coherence tomography of the human retina at 236,000 axial scans per second. Opt Lett 2007;32(14):2049–2051. [PubMed: 17632639]
- Huber R, Wojtkowski M, Taira K, Fujimoto JG, Hsu K. Amplified, frequency swept lasers for frequency domain reflectometry and OCT imaging: design and scaling principles. Opt Express 2005;13(9):3513–3528. [PubMed: 19495256]
- 26. Huber R, Wojtkowski M, Fujimoto JG. Fourier Domain Mode Locking (FDML): a new laser operating regime and applications for optical coherence tomography. Opt Express 2006;14(8):3225–3237. [PubMed: 19516464]
- 27. Donnelly WJ, Roorda A. Optimal pupil size in the human eye for axial resolution. J Opt Soc Am A Opt Image Sci Vis 2003;20(11):2010–2015. [PubMed: 14620328]
- 28. Hitzenberger CK, Trost P, Pak-Wai L, Qienyuan Z. Three-dimensional imaging of the human retina by high-speed optical coherence tomography. Opt Express 2003;11(21):2753–2761. [PubMed: 19471390]
- 29. Wojtkowski M, Bajraszewski T, Gorczynska I, et al. Ophthalmic imaging by spectral optical coherence tomography. Am J Ophthalmol 2004;138(3):412–419. [PubMed: 15364223]
- 30. Jiao SL, Knighton R, Huang XR, Gregori G, Puliafito CA. Simultaneous acquisition of sectional and fundus ophthalmic images with spectral-domain optical coherence tomography. Opt Express 2005;13 (2):444–452. [PubMed: 19488371]
- 31. Dandona L, Quigley HA, Brown AE, Enger C. Quantitative regional structure of the normal human lamina cribrosa: a racial comparison. Arch Ophthalmol 1990;108(3):393–398. [PubMed: 2310342]
- 32. Jonas JB, Mardin CY, Schlotzer-Schrehardt U, Naumann GO. Morphometry of the human lamina cribrosa surface. Invest Ophthalmol Vis Sci 1991;32(2):401–405. [PubMed: 1993592]
- 33. Gabriele ML, Ishikawa H, Wollstein G, et al. Peripapillary nerve fiber layer thickness profile determined with high speed, ultrahigh resolution optical coherence tomography high-density scanning. Invest Ophthalmol Vis Sci 2007;48(7):3154–3160. [PubMed: 17591885]
- 34. Povazay B, Bizheva K, Hermann B, et al. Enhanced visualization of choroidal vessels using ultrahigh resolution ophthalmic OCT at 1050 nm. Opt Express 2003;11(17):1980–1986. [PubMed: 19466083]
- 35. Unterhuber A, Povazay B, Hermann B, et al. In vivo retinal optical coherence tomography at 1040 nm-enhanced penetration into the choroid. Opt Express 2005;13(9):3252–3258. [PubMed: 19495226]
- 36. Povazay B, Hermann B, Unterhuber A, et al. Three-dimensional optical coherence tomography at 1050 nm versus 800 nm in retinal pathologies: enhanced performance and choroidal penetration in cataract patients. J Biomed Opt 2007;12(4):041211. [PubMed: 17867800]

37. Ferguson RD, Hammer DX, Paunescu LA, Beaton S, Schuman JS. Tracking optical coherence tomography. Opt Lett 2004;29(18):2139–2141. [PubMed: 15460882]

- 38. Hangai M, Jima Y, Gotoh N, et al. Three-dimensional imaging of macular holes with high-speed optical coherence tomography. Ophthalmology 2007;114(4):763–773. [PubMed: 17187861]
- 39. Podoleanu AG, Jackson DA. Combined optical coherence tomograph and scanning laser ophthalmoscope. Electron Lett 1998;34(11):1088–1090.
- Rogers JA, Podoleanu AG, Dobre GM, Jackson DA, Fitzke FW. Topography and volume measurements of the optic nerve using en-face optical coherence tomography. Opt Express 2001;9 (10):533–545. [PubMed: 19424371]
- 41. Podoleanu AG, Dobre GM, Cucu RG, et al. Combined multiplanar optical coherence tomography and confocal scanning ophthalmoscopy. J Biomed Opt 2004;9(1):86–93. [PubMed: 14715059]
- 42. Podoleanu AG, Dobre GM, Cucu RG, Rosen RB. Sequential optical coherence tomography and confocal imaging. Opt Lett 2004;29(4):364–366. [PubMed: 14971754]
- 43. van Velthoven ME, Verbraak FD, Yannuzzi LA, et al. Imaging the retina by en face optical coherence tomography. Retina 2006;26(2):129–136. [PubMed: 16467666]
- 44. Burgoyne CF, Downs JC, Bellezza AJ, Suh JK, Hart RT. The optic nerve head as a biomechanical structure: a new paradigm for understanding the role of IOP-related stress and strain in the pathophysiology of glaucomatous optic nerve head damage. Prog Retin Eye Res 2005;24(1):39–73. [PubMed: 15555526]
- 45. Tezel G, Trinkaus K, Wax MB. Alterations in the morphology of lamina cribrosa pores in glaucomatous eyes. Br J Ophthalmol 2004;88(2):251–256. [PubMed: 14736786]
- 46. Burgoyne CF, Downs JC, Bellezza AJ, Hart RT. Three-dimensional reconstruction of normal and early glaucoma monkey optic nerve head connective tissues. Invest Ophthalmol Vis Sci 2004;45(12): 4388–4399. [PubMed: 15557447]
- 47. Bhandari A, Fontana L, Fitzke FW, Hitchings RA. Quantitative analysis of the lamina cribrosa in vivo using a scanning laser ophthalmoscope. Curr Eye Res 1997;16(1):1–8. [PubMed: 9043817]
- 48. Fontana L, Bhandari A, Fitzke FW, Hitchings RA. In vivo morphometry of the lamina cribrosa and its relation to visual field loss in glaucoma. Curr Eye Res 1998;17(4):363–369. [PubMed: 9561827]
- 49. Maeda H, Nakamura M, Yamamoto M. Morphometric features of laminar pores in lamina cribrosa observed by scanning laser ophthalmoscopy. Jpn J Ophthalmol 1999;43(5):415–421. [PubMed: 10580665]
- 50. Vilupuru AS, Rangaswamy NV, Frishman LJ, et al. Adaptive optics scanning laser ophthalmoscopy for in vivo imaging of lamina cribrosa. J Opt Soc Am A Opt Image Sci Vis 2007;24(5):1417–1425. [PubMed: 17429488]
- 51. Pircher M, Gotzinger E, Hitzenberger CK. Dynamic focus in optical coherence tomography for retinal imaging. J Biomed Opt 2006;11(5):054013. [PubMed: 17092162]
- 52. Martinez-Conde S, Macknik SL, Hubel DH. The role of fixational eye movements in visual perception. Nat Rev Neurosci 2004;5(3):229–240. [PubMed: 14976522]

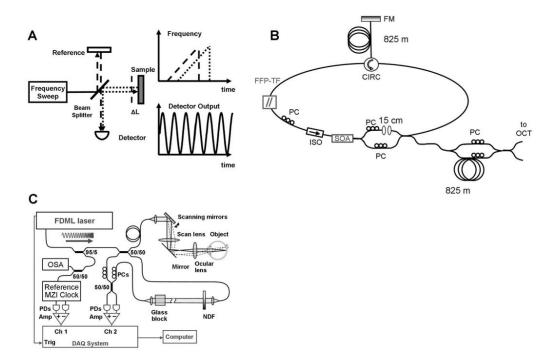


Figure 1. (A) Principles of swept-source OCT detection. (B) Diagram of a FDML laser used as the frequency swept light source. (C) Schematic of interferometer and OCT data acquisition used for retinal imaging. PC, polarization controller; ISO, isolator; CIRC, circulator; FM, Faraday mirror; FFP-TF, fiber Fabry-Perot tunable filter; SOA, semiconductor optical amplifier; PD, photodiode; OSA, optical spectrum analyzer; MZI, Mach-Zehnder interferometer; DAQ, data acquisition; NDF, neutral density filter.

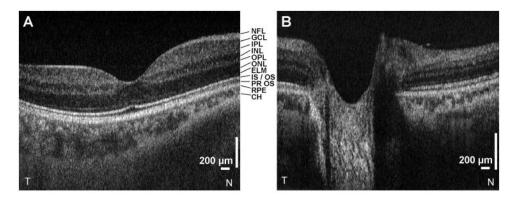


Figure 2. High-definition imaging of (A) the retina and (B) the optic nerve head. Beam diameter at cornea, 1.4 mm. Axial scans per image, 16,000. NFL, nerve fiber layer; GCL, ganglion cell layer; IPL, inner plexiform layer; INL, inner nuclear layer; OPL, outer plexiform layer; ONL, outer nuclear layer; ELM, external limiting membrane; IS/OS, photoreceptor inner segment/outer segment junction; PR OS, photoreceptor outer segments; RPE, retinal pigment epithelium; CH, choroid.

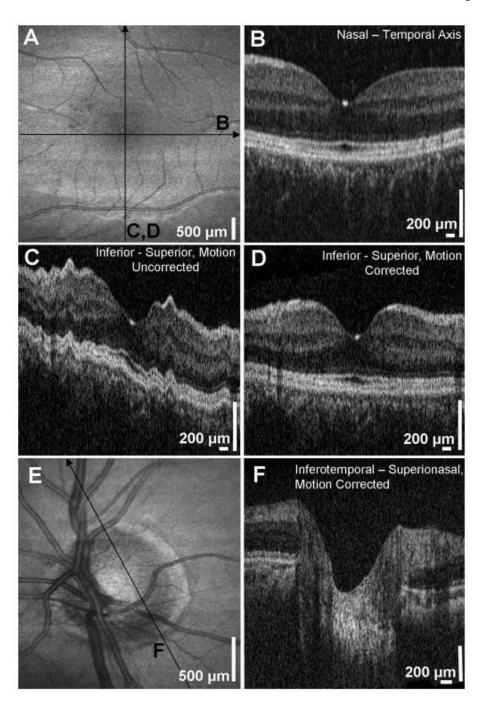


Figure 3.(**A**) OCT fundus image of the retina, without motion correction. (**B**) Slice through 3D OCT data set along the fast axis. (**C**) Slice through 3D OCT data set along the slow axis, showing the severity of axial motion. (**D**) Slice through 3D OCT data set along the slow axis, after correcting for axial motion. (**E**) OCT fundus image of the optic nerve head, without motion correction. (**F**) Oblique slice through 3D OCT data set, after correcting for axial motion. Beam diameter at cornea, 1.4 mm (**A**–**D**) and 2.9 mm (**E**–**F**). 512 × 850 axial scans.

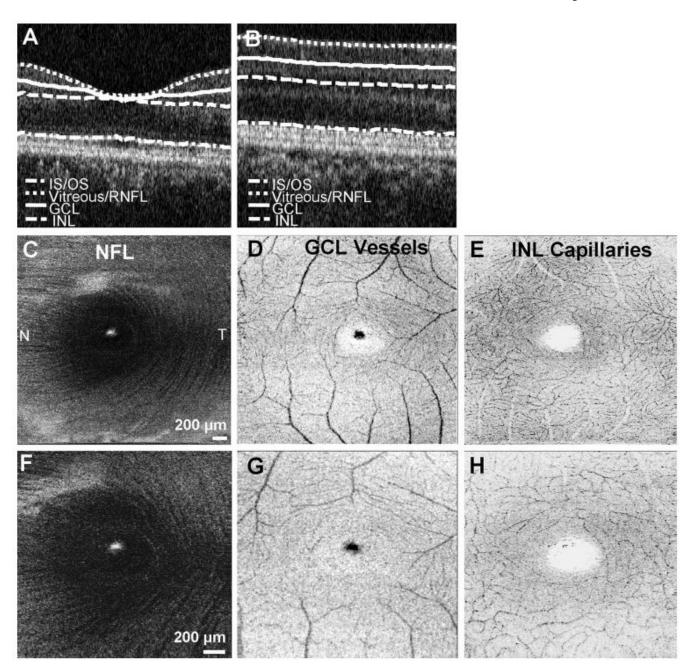


Figure 4. En face visualization of retinal layers. Processing a 3D OCT data set makes enhanced visualization of individual intraretinal layers possible. ($\bf A, B$) Different layers or boundaries are delineated and used to enhance visualization of anatomy. Imaging was performed over a 3 \times 3-mm ($\bf C$ - $\bf E$) and a 2 \times 2-mm ($\bf F$ - $\bf H$) field of view. En face visualizations of the ($\bf C, F$) nerve fiber layer (NFL), ($\bf D, G$) blood vessels in the ganglion cell layer (GCL), and ($\bf E, H$) capillary network of the inner nuclear layer (INL) is shown. Inner retinal vasculature images ($\bf D, E, G, H$) are displayed with an inverted grayscale. Beam diameter at cornea, 2.9 mm. 512 \times 850 axial scans.

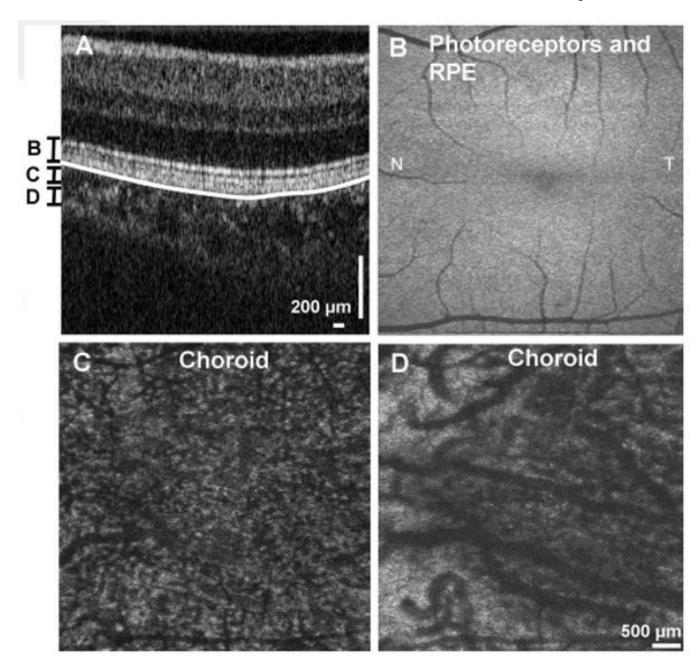


Figure 5. En face visualization of the outer retina and choroid in the macular region by axial integration of 3D OCT data. (A) Cross-sectional image showing the contour of Bruch's membrane (white line), and the axial integration ranges for (\mathbf{B} – \mathbf{D}). Shown are en face images of (\mathbf{B}) the photoreceptors and RPE; (\mathbf{C}) the choroid showing predominantly smaller vessels; (\mathbf{D}) of the choroid showing predominantly larger vessels. Beam diameter at cornea: 1.4 mm. 512 × 850 axial scans.

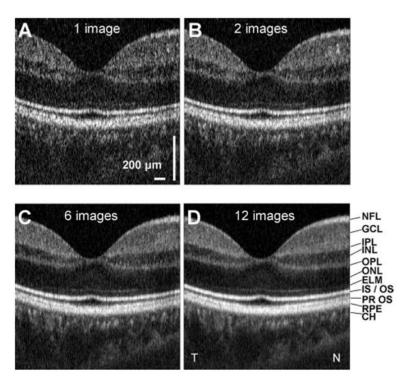


Figure 6. (A–D) Median filtering of OCT images improves visualization of the details of retinal layers. Although a dramatic improvement in visualization of intraretinal detail is seen by compounding two images (B) versus no compounding (A), little improvement is obtained by compounding 12 images (D) versus compounding 6 images (C). Beam diameter at cornea: $1.4 \text{ mm. } 512 \times 850 \text{ axial scans.}$

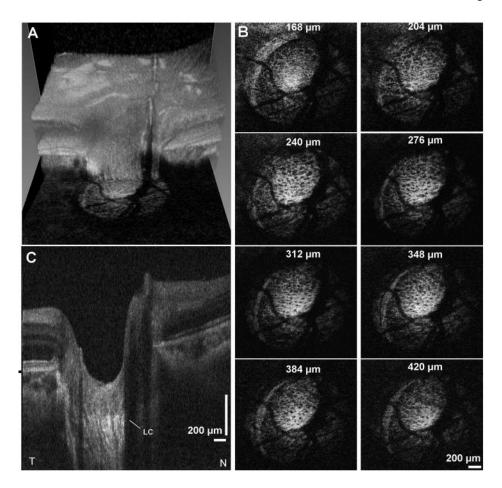


Figure 7. Imaging of the lamina cribrosa. (A) Images are interpolated onto en face planes through the 3D OCT data set at different depths relative to the RPE. (B) Interpolated images show the porous structure of the lamina cribrosa. Depths relative to Bruch's membrane are shown. (C) A series of six consecutive images compounded by median filtering along the slow axis shows enhanced visualization of deeper structures. The lamina cribrosa (LC) is clearly visible. Beam diameter at cornea: 1.4 mm. $512 \times 450 \text{ axial scans}$.